JOURNAL OF SYNCHROTRON RADIATION
ISSN 1600-5775

# Nondestructive imaging of the internal microstructure of vessels and nerve fibers in rat spinal cord using phase-contrast synchrotron radiation microtomography

Jianzhong Hu,[a] Ping Li,[a] Xianzhen Yin,[b] Tianding Wu,[a] Yong Cao,[a] Zhiming Yang,[a] Liyuan Jiang,[a] Shiping Hu[a] and Hongbin Lu[c]*

[a]Department of Spine Surgery, Xiangya Hospital, Central South University, Changsha 410008, People's Republic of China, [b]Shanghai Institute of Materia Medica, Chinese Academy of Sciences, Shanghai 200135, People's Republic of China, and [c]Department of Sports Medicine, Research Centre of Sports Medicine, Xiangya Hospital, Central South University, Changsha 410008, People's Republic of China. *Correspondence e-mail: hongbinlu@hotmail.com

Received 6 May 2016
Accepted 4 January 2017

Edited by P. A. Pianetta, SLAC National Accelerator Laboratory, USA

**Keywords:** synchrotron radiation imaging; virtual slices; three-dimensional microstructure; phase-contrast imaging; spinal cord.

The spinal cord is the primary neurological link between the brain and other parts of the body, but unlike those of the brain, advances in spinal cord imaging have been challenged by the more complicated and inhomogeneous anatomy of the spine. Fortunately with the advancement of high technology, phase-contrast synchrotron radiation microtomography has become widespread in scientific research because of its ability to generate high-quality and high-resolution images. In this study, this method has been employed for nondestructive imaging of the internal microstructure of rat spinal cord. Furthermore, digital virtual slices based on phase-contrast synchrotron radiation were compared with conventional histological sections. The three-dimensional internal microstructure of the intramedullary arteries and nerve fibers was vividly detected within the same spinal cord specimen without the application of a stain or contrast agent or sectioning. With the aid of image post-processing, an optimization of vessel and nerve fiber images was obtained. The findings indicated that phase-contrast synchrotron radiation microtomography is unique in the field of three-dimensional imaging and sets novel standards for pathophysiological investigations in various neurovascular diseases.

## 1. Introduction

Although the spinal cord is the most important information pathway connecting the brain and the peripheral nervous system, spinal cord imaging is still at an early stage of development and clinical implementation. Therefore it is necessary to look for better imaging techniques that provide relatively reliable and reproducible physiologic information about the imaged tissue.

Recently, various methods, including histopathology, confocal microscopy, magnetic resonance imaging (MRI) and computed tomography (CT), have been used to assess the spinal cord condition (Talbott *et al.*, 2015; Long *et al.*, 2014). Immunohistological analysis and confocal microscopy may achieve a higher resolution *via* the use of specific antibodies directed against tissues and cells (Dong *et al.*, 2008; Li *et al.*, 2011). However, histological methods are destructive and only provide two-dimensional images. Three-dimensional (3D) information is difficult to obtain from independent sections. Moreover, confocal microscopy only acquires 3D and four-dimensional information for samples of depth less than 50 µm. In addition, thin-sectioning and staining processes result in

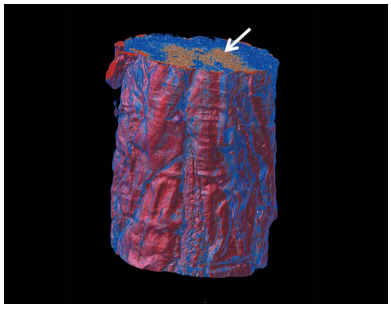

tissue shrinkage and geometric distortion, and the process is typically time-consuming.

Consequently, interest in alternative methods applicable to any type of tissue continue to increase. High-resolution MRI and X-ray micro-computed tomography (μCT) for the nondestructive microscopic analysis of tissue specimens has recently been proposed (Zhao *et al.*, 2015; Foxley *et al.*, 2015). The structure of both normal and injured animal spinal cords with different damage, such as weighted drop injury (Nevo *et al.*, 2001; Gonzalez-Lara *et al.*, 2009; Fradet *et al.*, 2014) and myelin-deficient tissues (Cohen-Adad *et al.*, 2012), exhibited excellent contrast between gray and white matter *via* diffusion MRI (Kumar *et al.*, 2014). However, the *ex vivo* diffusion tensor imaging (DTI) data acquisition process is typically time-consuming and often requires more than 24 h (Gulani *et al.*, 2001). In addition, high-field and small-bore MRI remain relatively expensive and difficult to set up and maintain. Moreover, the other limits of high-field MRI have been the magnetic field in homogeneity-induced image distortions. X-ray μCT imaging has been performed *ex vivo* and *in vivo* (Lussani *et al.*, 2015). The μCT imaging technique is simpler compared with MRI and has been demonstrated to be an effective tool for imaging bone. In contrast, soft-tissue imaging is typically impossible *via* μCT without the use of X-ray-absorbing contrast agents because of the differences in the smaller densities and X-ray absorption of different tissue structures. Moreover, water-soluble contrast agents are frequently used in humans; however, several factors have restricted their application in small animals: firstly, μCT technology is not as rapid in capturing images as human CT imaging, with acquisition times between 10 and 20 min in animals *versus* seconds in humans (Martiniova *et al.*, 2010); secondly, the water-soluble contrast agents are cleared faster in small animals compared with humans; thus, the time is insufficient to acquire μCT images.

In recent years, the development of more advanced microscopic radiography, particularly the advent of the synchrotron radiation (SR) light source, has added a novel dimension regarding the use of μCT in small-animal imaging. SR light sources, having the characteristic of tunable high-flux-density monochromatic beams, may meet the needs of CT of biosamples at the micrometer level (Liu *et al.*, 2010). In addition to conventional absorption imaging, SR phase-contrast imaging is based on the visualization of the wavefront changes when radiation passes through an object (Bravin *et al.*, 2013). It is also the simplest imaging method for visualizing soft-tissue microstructure based on phase effects due to variations in refractive indices by increasing the distance between the sample and the detector (Dullin *et al.*, 2015). Moreover, compared with μCT, SR phase-contrast micro-tomography (PCT) has a greater spatial resolution to illustrate the density contrast between soft tissues. These characteristics make PCT with SR as light source well suited for investigating the 3D configuration of specific biological samples [*e.g.* bone and bone tendon microstructures, spinal cord micro-vascular network, the kidney, the liver, pulmonary and cerebral angioarchitecture (Hesse *et al.*, 2015; Lu *et al.*, 2015; Hu *et al.*, 2014; Li *et al.*, 2013; Lin *et al.*, 2015; Zhang *et al.*, 2014; Velroyen *et al.*, 2014)] without contrast agents. In addition, X-ray PCT also had been applied to obtain 3D structural information of mouse fetus, pancreatic and zebrafish muscle (Tapfer *et al.*, 2013; Hoshino *et al.*, 2012; Vågberg *et al.*, 2015). These previous reports have suggested that the SR-PCT system without a contrast agent has the potential for more widespread application compared with the micro-MRI and conventional μCT systems. Thus, we first used SR-PCT without a contrast agent to determine the microstructure of rat spinal cord with intact tissues.

The current study aimed to determine whether an approach that involves SR phase-contrast imaging yields images with useful gray matter and white matter contrasts that clearly demonstrate the detailed microscopic anatomic structures of rat spinal cord.

## 2. Materials and methods

### 2.1. Animal preparation

The study was approved by the Animal Welfare Committee of Central South University. Twelve Sprague-Dawley male rats (250–300 g) were randomly divided into A and B groups ($n$ = 6 per group). The rats were deeply anesthetized with an overdose of 10% chloral hydrate intraperitoneally (400 mg kg$^{-1}$). The circulatory system was rapidly and sufficiently perfused using heparinized saline *via* the aorta ascendens and provided an effective drain for blood flow. Ten-percent buffered formalin was subsequently perfused for tissue fixation. All perfusion solutions were preheated, and the operation was conducted in a warm environment. All animals were subsequently maintained in a 4°C refrigerator overnight. The next day, the rats underwent a laminectomy centered at the tenth thoracic vertebra, and a 6 mm length of the spinal cord was removed; graded ethanol was used to dehydrate the samples. The samples in group A, which were immersed in methylsalicylate for 24–48 h, were used for SR μCT; the samples in group B underwent histological examination using an optical microscope.

### 2.2. SR-PCT scanning, phase retrieval and 3D rendering

SR-PCT scanning was performed on a BL13W1 beamline at the Shanghai Synchrotron Radiation Facility (SSRF) in China. The energy levels varied from 8 to 72.5 keV, and the maximal beam size was 5 mm (vertical) × 48 mm (horizontal) at the object position at 20 keV, with a divergence of 0.2 mrad (vertical) × 1.5 mrad (horizontal). The beam energy was set to 15.0 keV, and the sample-to-detector distance was adjusted to 30 cm to obtain the optimal image. The sample was placed at the center of the rotary stage to enable a 180° rotation during the μCT scanning. Seven hundred and twenty initial projection images were captured *via* the CCD detector, and the pixel size was 3.25 μm × 3.25 μm. Then phase retrieval was applied to the individual projections to convert the phase-contrast fringes into phase-based area contrast, according to an estimate of the phase-attenuation ratio (often termed '$\delta\beta$/-ratio'),

which was based on a 'single distance' phase-retrieval algorithm by Paganin *et al.* (2002). Furthermore, the total projected images were transformed into digital slice sections using the fast slice reconstruction software compiled by the BL13W1 experimental station of SSRF, which was based on the FBP algorithm (Kak & Slaney, 1988). A series of two-dimensional transverse slices were subsequently rendered into a 3D presentation using *Amira* reconstruction software (Visage Imaging, Australia). The algorithms previously described by Lee *et al.* (1994) were used to generate 3D pseudo colored images of the spinal cord micro-vasculature. The vascular number, cord cross-section area (CSA), gray matter CSA and white matter CSA were obtained by NIH image analysis software *ImageJ*.

### 2.3. Hematoxylin and eosin staining observation and quantitative analysis

To investigate the morphology of the spinal cord microstructure in rats, the samples in group B were post-fixed in 4% buffered formalin overnight and cryo-protected in 30% sucrose for 48 h. Then the samples were embedded in paraffin, and two-plane images of slices with a 10 µm thickness (transverse, sagittal) were obtained. All sections were processed for hematoxylin and eosin (H&E) staining. Spinal cord microstructure images were examined and photographed with an optical microscope (Leica DM4000B, Germany); the images were subsequently compared with 3D images *via* SR phase imaging. Then the area of white and gray matter in each section was quantified using NIH image analysis software *ImageJ*.

### 2.4. Statistical analyses

All data are presented as mean ± standard error of the mean unless otherwise specified. Data were analysed using the variance test and independent samples *t*-test, while cord CSA values measured by H&E staining and SR-PCT were analyzed by correlation analysis; $p < 0.05$ was considered as statistically significant.

## 3. Results

### 3.1. Reconstruction of the 3D spinal cord microstructure and virtual tissue sections

In terms of a stereoscopic effect, 3D images of the spinal cord microstructure were obtained using reconstructed CT slices. The butterfly outline of the spinal cord (white arrow) may also be easily distinguished in the 3D rendered images (Fig. 1). Moreover, the detailed microstructure of the spinal cord may be obtained from the different angles and/or perspectives of 3D rendered images (Figs. 2*b* and 2*c*). Compared with the cross-sectional schematic view of the spinal cord (Fig. 2*a*), the white matter (red dovetail arrow), gray matter (white dovetail arrow), vasculature (blue arrow) and central canal (black arrow) were distinguishable in the virtual tissue sections, and the morphology of the spinal cord

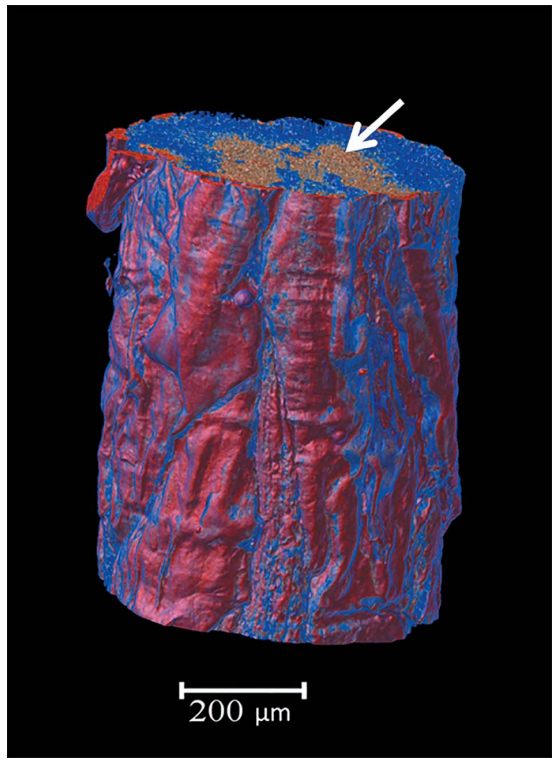


**Figure 1**
3D reconstructed rat spinal cord imaging. The microstructure of the spinal cord may be clearly visualized, and the white arrow indicates the butterfly area of the spinal cord.

in the cross-section virtual tissue slice was also consistent with the schematic view.

### 3.2. Comparison of SR images and H&E staining of the spinal cord

Information regarding the spinal cord microstructure may be visualized in greater detail using virtual tissue slices with characteristic coloring. We easily observed the spinal cord micro-vascular network (red arrow) and central canal (black thick arrow) as well as the white matter (red dovetail arrow) and gray matter (white dovetail arrow) in the virtual slices (Figs. 3*c* and 3*d*). The reconstructed slices from the normal rats and their corresponding H&E-stained sections (Figs. 3*a* and 3*b*) were compared. The results of the 3D rendering images were consistent with the possibility that the tissue integrity was compromised as a result of the sample preparation for the histological staining. Thus, the vascular distribution and structure of the spinal cord were investigated in greater detail using the SR technique. Quantitative analysis shows that rat spinal cord CSAs were about 5.83 ± 0.62 *versus* 6.22 ± 0.4 $mm^2$ at the tenth thoracic level by H&E staining and SR-PCT, respectively. The white matter CSA was 4.82 ± 0.67 *versus* 5.11 ± 0.4 $mm^2$, the gray matter CSA was 1.01 ± 0.13 *versus* 1.11 ± 0.14 $mm^2$ (Table 1, Fig. 3*e*). Furthermore, correlation analysis showed that SR-PCT detection was significantly associated with H&E staining quantitative analysis (Fig. 3*f*).

### 3.3. Spinal cord vascular and visualization

Simultaneous 3D imaging of the micro-vascular network and microstructure in rat spinal cord may be performed using the SR technique (Fig. 4*a*). Using the virtual tissue sections, we determined that most tiny vessels were distributed in the gray matter, which is similar to a previous study (Cao *et al.*, 2015). Furthermore, the spinal cord vasculature may be determined using 3D reconstruction imaging (Figs. 4*b* and 4*c*). The gradation of the coloring used in the figure labeled the natural distribution of the spinal cord micro-vessels within the specific range examined (Fig. 4*d*); the quantitative analysis of the vascular number based on the different diameter vessels indicates that the diameters of most spinal cord micro-vessels

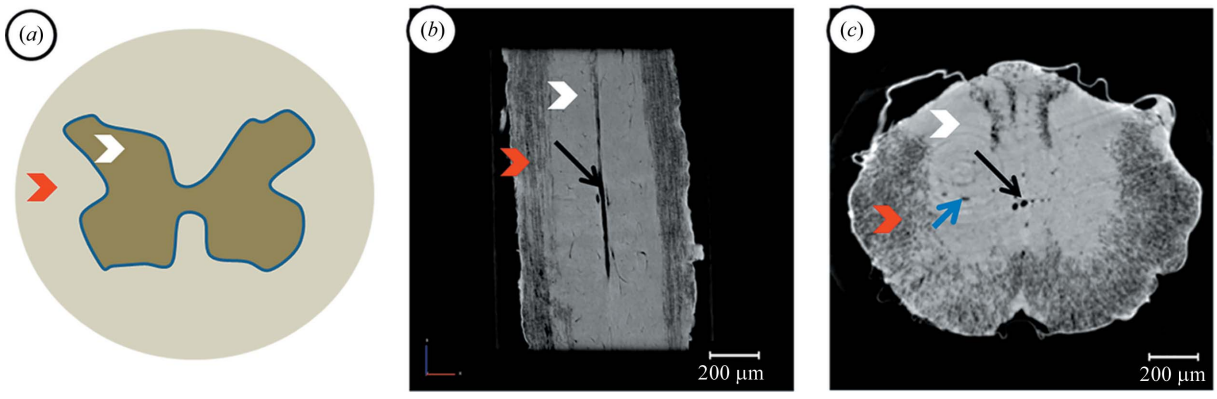


**Figure 2**
Virtual tissue slice based on spinal cord 3D rendering. (*a*) Based on the cross-sectional schematic view, the spinal cord is composed of a butterfly area, referred to as gray matter, and white matter. (*b*, *c*) The spinal cord white matter, gray matter, vasculature and central canal are distinguishable in the virtual tissue slices from different perspectives (transverse, sagittal). The blue arrow indicates the micro-vascular of the spinal cord, the black arrow indicates the central canal, the red dovetail arrow indicates the white matter and the white dovetail arrow indicates the gray matter in the spinal cord.

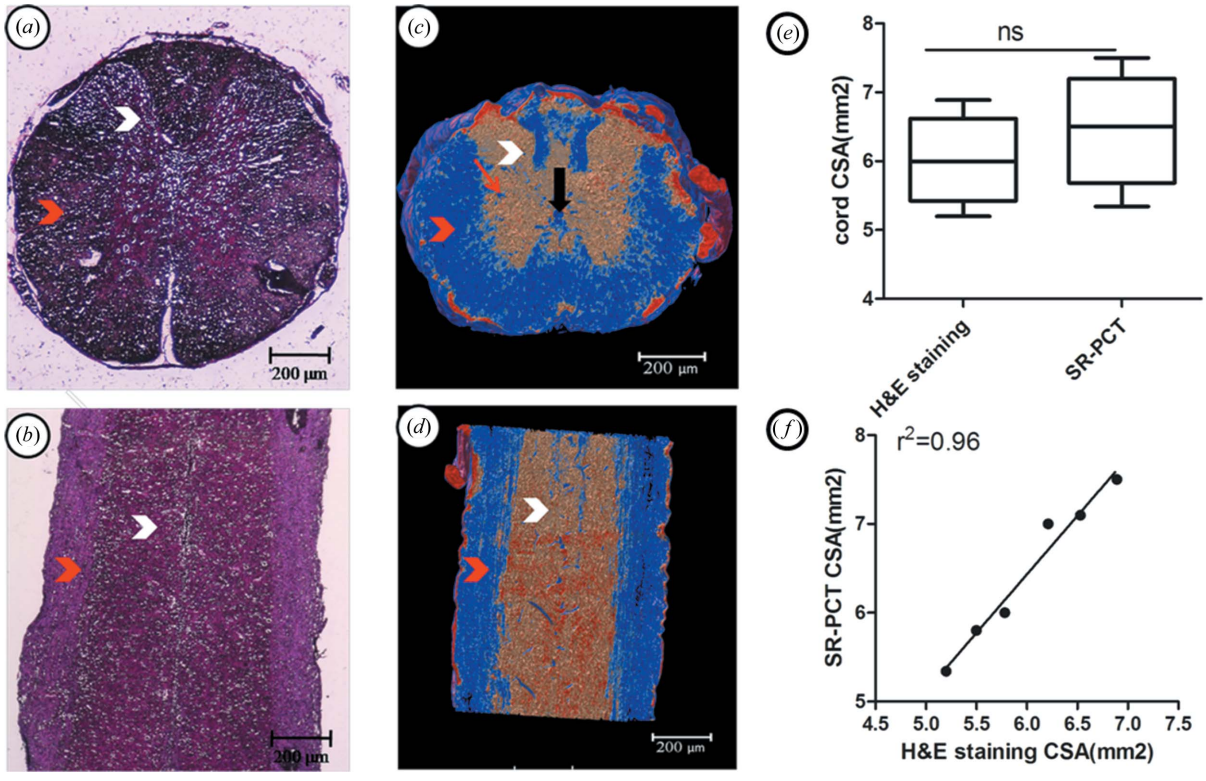


**Figure 3**
After characteristic coloring, the virtual tissue slices were compared with H&E stained slices. (*a*, *b*) Spinal cord coronal and sagittal plane H&E staining. (*c*, *d*) Transverse and vertical virtual tissue slices based on microstructure 3D reconstruction of the spinal cord. The red arrow indicates the micro-vasculature of the spinal cord, the black broad arrow indicates the central canal, the red dovetail arrow indicates the white matter and the white dovetail arrow indicates the gray matter in the spinal cord. (*e*) Average cord cross-sectional area ($mm^2$) in tissue sections (10 per animal) at the tenth thoracic level ($n$ = 6 animals per group). (*f*) Correlation analysis of measured cord cross-sectional areas (CSAs) by using SR-PCT and H&E staining at the matched level.

**Table 1**
Rat spinal cord cross-sectional area (CSA) measured at the tenth thoracic level by H&E staining and SR-PCT.

| Method | Level | Cord CSA ($mm^2$) | White matter CSA ($mm^2$) | Gray matter CSA ($mm^2$) | Gray matter fraction (%) |
|---|---|---|---|---|---|
| H&E staining | T10 | 5.83 ± 0.62 | 4.82 ± 0.67 | 1.01 ± 0.13 | 17.3 |
| SR-PCT | T10 | 6.22 ± 0.4 | 5.11 ± 0.4 | 1.11 ± 0.14 | 17.8 |

are less than 40 µm (Fig. 4*e*); however, the histological staining is not obtained.

### 3.4. Spinal cord white matter extraction and 3D reconstruction

Compared with the histological staining, we may not only distinguish the spinal cord microstructure and micro-vascular network but also extract the spinal cord white matter and 3D rendering; thus, we may easily observe the morphology of the white matter. We initially selected the region of interest (ROI) in the white matter (Fig. 5*a*); the ROI of the white matter in the spinal cord as well as the micro-vascular network may be 3D reconstructed using *Amria* software (Figs. 5*b* and 5*c*). The 3D image of the ROI in the white matter of the spinal cord is shown in Fig. 5(*d*). Furthermore, using the magnification image of the white matter (Fig. 5*e*), we determined that the white matter in the spinal cord consisted of many parallel arrangement bundle structures.

## 4. Discussion

In recent years, histological experiments have been considered a common and useful method for visualizing the spinal cord microstructure (Myojin *et al.*, 2007). However, there are many disadvantages in the corrosion cast method. For example, it is invasive, complex, has limited vision for analysis and may involve the overlapping of structures in the planar view. Furthermore, MRI and CT imaging were subsequently

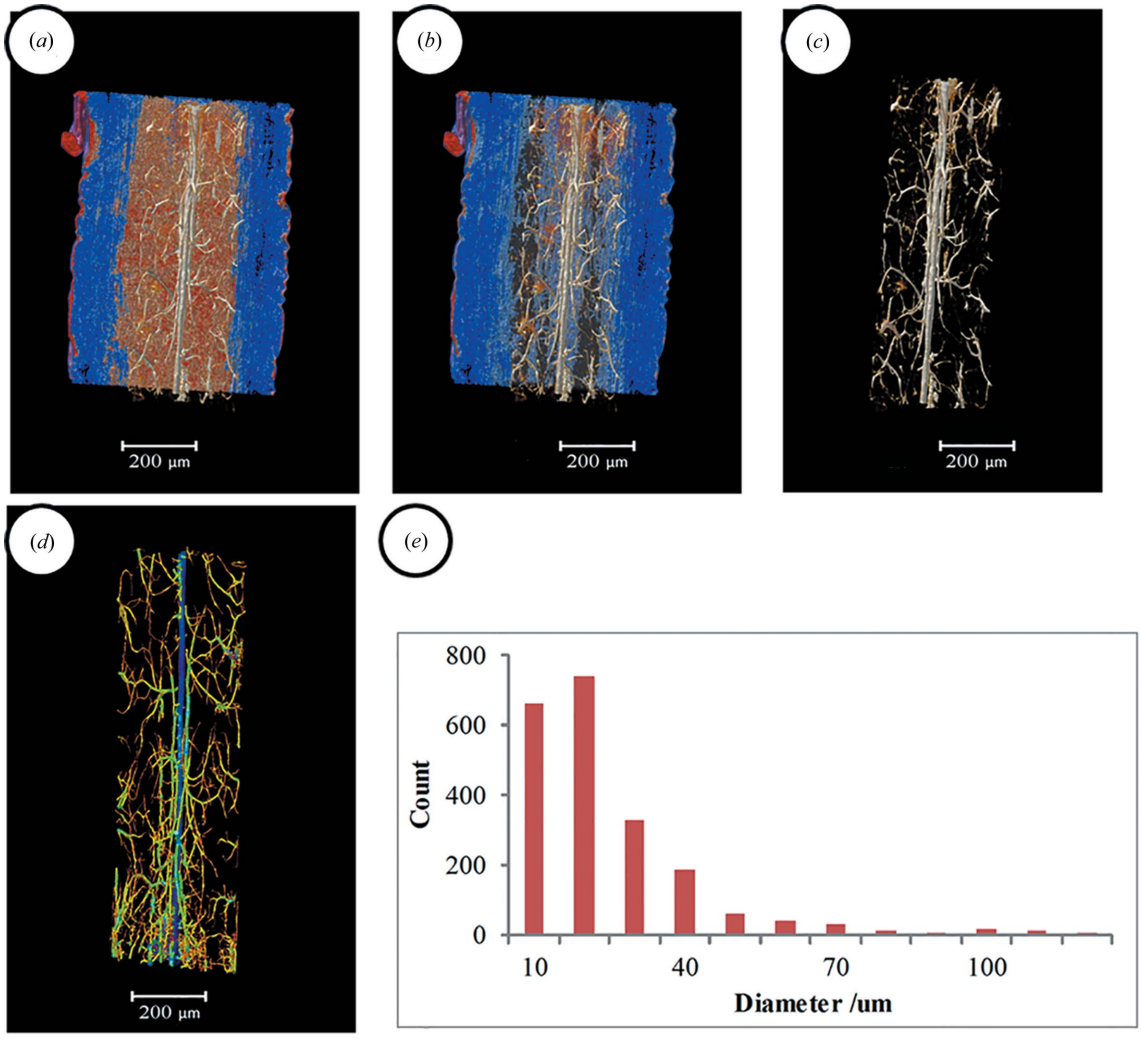


**Figure 4**
Spinal cord vascular visualization and 3D characteristic labeling. (*a*) Simultaneous 3D imaging of the micro-vascular network and microstructure in rat spinal cord using the SR technique. (*b*) Most tiny vessels are distributed in the gray matter from longitudinal virtual tissue sections. (*c*) The 3D micro-vascular network extracted from (*b*). (*d*) A clear framework for 3D characteristic labeling of the spinal cord vasculature based on the different diameters of the vessels. (*e*) Quantitative analysis of the vascular number or diameter is demonstrated.

considered new and ideal nondestructive techniques for observing detailed spinal cord microstructure. However, as a result of the weak inherent differential contrast of the gray levels between the soft tissues, the microstructure of rat spinal cord is not easily detected *via* conventional CT without contrast agent perfusion or MRI. Several limitations have also impaired their widespread use. For example, the MRI process is complex and time-consuming, and it is difficult to obtain sufficient details in animals (Bonny *et al.*, 2004). Regarding μCT (Ford *et al.*, 2003), the imaging depends on the distribution of contrast agents; in addition, the μCT method lacks a sufficient resolution to detect the microstructure in the rat spinal cord.

In the present study, we used a novel technique to identify the spinal cord microscopic anatomic structures without a contrast agent *ex vivo* in rats. Thus, the development of a higher-spatial-resolution imaging technique has been advanced by physioptical development; 3D spinal cord images with a useful delineation of the gray matter, white matter, dorsal horn, ventral horn and vessels may be obtained using SR-PCT without a contrast agent, which is comparable with H&E sections. We subsequently confirmed that the SR phase imaging method has potential for the assessment of the spinal cord microarchitecture in rats. Interestingly, a recent study also has shown that SR imaging can visualize the micro-vascular network and the neuronal system in a mouse spinal cord (Fratini *et al.*, 2015). However, a contrast agent was used to visualize the micro-vascular network in the study, such that simultaneous imaging of the micro-vascular network and microstructure of spinal cord was not obtained on one sample by single scanning. In contrast, simultaneous imaging micro-vascular network and microstructure can be achieved by single scanning in our study since vascular imaging was not dependent on contrast agent.

Synchrotron radiation X-rays are emitted from electrons when curvilinear movement induces a change in their direction near the speed of light, which may be controlled by the magnetic field in a storage ring and is quite distinct from the generation of traditional X-rays following the bombardment of a metal anode with electrons (Shirai *et al.*, 2013). As a result of the characteristics of high directionality, small divergence and variable polarization compared with micro-CT and MRI,

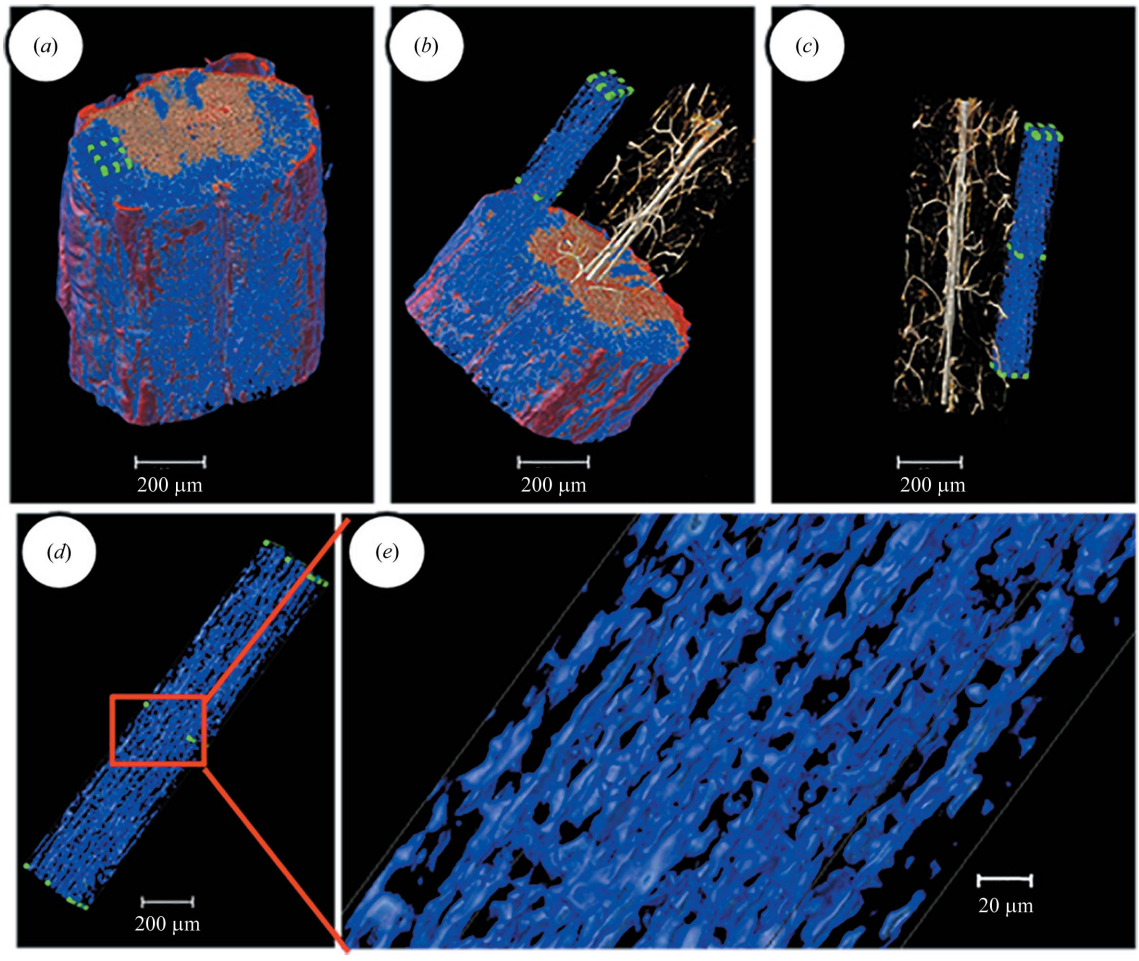


**Figure 5**
Spinal cord white matter extraction and 3D reconstruction. (*a*) The ROI of the white matter was selected in the 3D imaging of the spinal cord. The green area indicates the ROI. (*b*, *c*) The ROI of the white matter as well as the micro-vasculature of the spinal cord may be extracted from 3D imaging of the spinal cord. (*d*) 3D image of the ROI in the white matter of the spinal cord. (*e*) Magnified image of the red square in (*d*); the white matter of the spinal cord consists of many parallel arrangement bundle structures.

phase imaging using a SR X-ray source may acquire a higher resolution (Margaritondo & Meuli, 2003). This novel experimental modality maintains sample integrity and omits the complicated sample preparation procedures required for conventional methods. In addition, the datasets may be extracted and analyzed from different angles and at multiple levels, which has been impossible using conventional histological methods. It is noteworthy that the SR phase imaging technique provides a novel and promising approach for the direct visualization of microscopic structures in the spinal cord. The use of SR phase imaging enables gray matter and white matter to be distinguished as well as the visualization of the spinal cord micro-vasculature and nerve fiber. Thus, this method is more accurate, convenient and intuitive for evaluations of the extent of spinal cord parenchyma injury, micro-vascular lesions and prognosis. Consequently, it is expected to be a promising tool that enables the rapid performance of spinal cord disease investigations in clinical radiology. In the future, we hope to observe the interactions of the spinal cord parenchyma and micro-vascular network as well as investigate the size of the cavity of the spinal cord following a spinal cord injury *via* SR phase imaging.

On the other hand, the anatomy of the spinal cord is established but remains somewhat obscured by present-day radiological standards. In animal studies or *ex vivo* imaging, the cord anatomy has not been properly visualized for low resolution and contrast of traditional imaging methods, such as MRI with resolution about 10 mm, μCT at 8 mm and high-frequency ultrasound biomicroscopy (UBM) with spatial resolution of 30–50 mm (Cleary *et al.*, 2011; Johnson *et al.*, 2006; Phoon, 2006). However, SR-PCT, having a spatial resolution of about 7.4 μm, has the potential to identify small-scale lesions or structures that may relate to neurological deficits and allows detailed anatomical imaging and tissue segmentation. In addition, SR-PCT has higher soft-tissue contrast than other imaging methods (Bravin *et al.*, 2013). Therefore, the 3D images of the micro-vascular network and microstructure in rat spinal cord can be simultaneously obtained, so that the interrelation between spinal cord microstructure and micro-vascular networks can be revealed from a 3D perspective. Then it can also be a more accurate and intuitive method for uncovering anatomical mechanisms of various neurovascular diseases. During the past, absorption imaging had been considered as the gold standard to observe vascular morphology. However, the quality of absorption imaging often depends on the size of the contrast agent, volume and perfusion pressure (Shirai *et al.*, 2013), such that anatomical structures of the spinal micro-vascular network are often partly missing for blocking and/or bursting micro-vascular by contrast agents. Fortunately, unlike absorption imaging, contrast agent was not needed in the process of SR phase-contrast imaging. Therefore, relative to absorption imaging, more detailed information about anatomical structures of the spinal micro-vascular network can be obtained.

Nevertheless, several limitations exist regarding this novel imaging technique. First, it is difficult to acquire images of a large area due to the narrow light spot. Thus, the sample size must be sufficiently small to be contained in the entire visual field. Second, an X-ray source that provides high intensity, polarization, good coherence and small divergence is necessary for phase-contrast imaging. However, to date, only the sophisticated SR light source or micro-focus X-ray source have met these requirements. Furthermore, the instrumentation required for SR X-ray generation and imaging is complex and expensive; thus, it may not be widely available. Finally, to some extent, the accuracy of microscopic structure reconstruction may be affected by the shrinkage of spinal cord tissue as a result of the dehydration that occurs during the scanning procedure.

Although SR has several disadvantages, SR phase imaging provides simultaneous 3D imaging of the micro-vascular network and microstructures in rat spinal cord. Thus, it is anticipated that, in the near future, synchrotron techniques will substantially increase our understanding of the interactions in the spinal cord microstructure and the micro-vascular network that occur *in vivo* for several pathologies. Furthermore, we hypothesize that SR-based techniques will provide valuable insights into the underlying pathological mechanisms of spinal cord injury and neurodegenerative diseases.

In conclusion, for the first time, we have presented the 3D morphological features of microscopic structures in rat spinal cord using SR-based phase imaging without contrast agents. As a result, spinal cord microstructures were distinguished at an unprecedented resolution. Thus, this technique has the potential to be a powerful tool for the comprehensive characterization of physiological and pathophysiological characteristics of spinal cord diseases. Furthermore, it is anticipated that future studies using SR imaging will demonstrate the capacity for this technique to provide a more efficient evaluation of therapeutic strategies.

## Acknowledgements

The authors would like to thank Dr Tiqiao Xiao and other staff at the BL13W1 station of the Shanghai Synchrotron Radiation Facility (SSRF), Shanghai, China, for their kind assistance during the experiments. The study was financially supported by the National Natural Science Foundation of China, Beijing, China (Nos. 81171698, 81301542 and 81371956). Finally, we would like to claim that a medical writer from American Journal Experts helped to prepare the manuscript before submission.

## References

Bonny, J. M., Gaviria, M., Donnat, J. P., Jean, B., Privat, A. & Renou, J. P. (2004). *Neurobiol. Dis.* **15**, 474–482.
Bravin, A., Coan, P. & Suortti, P. (2013). *Phys. Med. Biol.* **58**, R1–35.
Cao, Y., Wu, T., Yuan, Z., Li, D., Ni, S., Hu, J. & Lu, H. (2015). *Sci. Rep.* **5**, 12643.
Cleary, J. O., Modat, M., Norris, F. C., Price, A. N., Jayakody, S. A., Martinez-Barbera, J. P., Greene, N. D., Hawkes, D. J., Ordidge, R. J., Scambler, P. J., Ourselin, S. & Lythgoe, M. F. (2011). *NeuroImage*, **54**, 769–778.
Cohen-Adad, J., Zhao, W., Wald, L. L. & Oaklander, A. L. (2012). *Neurology*, **79**, 2217.

Dong, M., Liu, R., Guo, L., Li, C. & Tan, G. (2008). *APMIS*, **116**, 972–984.
Dullin, C., dal Monego, S., Larsson, E., Mohammadi, S., Krenkel, M., Garrovo, C., Biffi, S., Lorenzon, A., Markus, A., Napp, J., Salditt, T., Accardo, A., Alves, F. & Tromba, G. (2015). *J. Synchrotron Rad.* **22**, 143–155.
Ford, N. L., Thornton, M. M. & Holdsworth, D. W. (2003). *Med. Phys.* **30**, 2869–2877.
Foxley, S., Domowicz, M., Karczmar, G. S. & Schwartz, N. (2015). *Med. Phys.* **42**, 1463–1472.
Fradet, L., Arnoux, P. J., Ranjeva, J. P., Petit, Y. & Callot, V. (2014). *Spine*, **39**, E262–E269.
Fratini, M., Bukreeva, I., Campi, G., Brun, F., Tromba, G., Modregger, P., Bucci, D., Battaglia, G., Spanò, R., Mastrogiacomo, M., Requardt, H., Giove, F., Bravin, A. & Cedola, A. (2015). *Sci. Rep.* **5**, 8514.
Gonzalez-Lara, L. E., Xu, X., Hofstetrova, K., Pniak, A., Brown, A. & Foster, P. J. (2009). *J. Neurotrauma*, **26**, 753–762.
Gulani, V., Webb, A. G., Duncan, I. D. & Lauterbur, P. C. (2001). *Magn. Reson. Med.* **45**, 191–195.
Hesse, B., Varga, P., Langer, M., Pacureanu, A., Schrof, S., Männicke, N., Suhonen, H., Maurer, P., Cloetens, P., Peyrin, F. & Raum, K. (2015). *J. Bone Miner. Res.* **30**, 346–356.
Hoshino, M., Uesugi, K. & Yagi, N. (2012). *Biol. Open*, **1**, 269–274.
Hu, J., Cao, Y., Wu, T., Li, D. & Lu, H. (2014). *Med. Phys.* **41**, 101904.
Johnson, J. T., Hansen, M. S., Wu, I., Healy, L. J., Johnson, C. R., Jones, G. M., Capecchi, M. R. & Keller, C. (2006). *PLOS Genet.* **2**, e61.
Kak, A. C. & Slaney, M. (1988). *Principles of Computerized Tomographic Imaging.* New York: IEEE.
Kumar, M., Duda, J. T., Hwang, W. T., Kenworthy, C., Ittyerah, R., Pickup, S., Brodkin, E. S., Gee, J. C., Abel, T. & Poptani, H. (2014). *PLoS One*, **9**, e109872.
Lee, T., Kashyap, R. L. & Chu, C. (1994). *Graph. Models Image Processing*, **56**, 462–478.
Li, B. L., Zhou, B., Wu, W. Z., Zhang, Y. Q., Du, G. H., Shi, H. C. & Chen, S. L. (2013). *Chin. J. Hepatol.* **21**, 684–687.
Li, H., Paes de Faria, J., Andrew, P., Nitarska, J. & Richardson, W. D. (2011). *Neuron*, **69**, 918–929.
Lin, H., Kou, B., Li, X., Wang, Y., Ding, B., Shi, C., Liu, H., Tang, R., Sun, J., Yan, F. & Zhang, H. (2015). *PLoS One*, **10**, e121438.
Liu, X., Zhao, J., Sun, J., Gu, X., Xiao, T., Liu, P. & Xu, L. X. (2010). *Phys. Med. Biol.* **55**, 2399–2409.
Long, H. Q., Xie, W. H., Chen, W. L., Xie, W. L., Xu, J. H. & Hu, Y. (2014). *Int. J. Mol. Sci.* **15**, 12061–12073.
Lu, H., Zheng, C., Wang, Z., Chen, C., Chen, H. & Hu, J. (2015). *PLoS One*, **10**, e124724.
Lussani, F. C., Vescovi, R. F. da C., de Souza, T. D., Leite, C. A. & Giles, C. (2015). *Rev. Sci. Instrum.* **86**, 063705.
Margaritondo, G. & Meuli, R. (2003). *Eur. Radiol.* **13**, 2633–2641.
Martiniova, L., Schimel, D., Lai, E. W., Limpuangthip, A., Kvetnansky, R. & Pacak, K. (2010). *Methods*, **50**, 20–25.
Myojin, K., Taguchi, A., Umetani, K., Fukushima, K., Nishiura, N., Matsuyama, T., Kimura, H., Stern, D. M., Imai, Y. & Mori, H. (2007). *Am. J. Neuroradiol.* **28**, 953–957.
Nevo, U., Hauben, E., Yoles, E., Agranov, E., Akselrod, S., Schwartz, M. & Neeman, M. (2001). *Magn. Reson. Med.* **45**, 1–9.
Paganin, D., Mayo, S. C., Gureyev, T. E., Miller, P. R. & Wilkins, S. W. (2002). *J. Microsc.* **206**, 33–40.
Phoon, C. K. (2006). *Pediatr. Res.* **60**, 14–21.
Shirai, M., Schwenke, D. O., Tsuchimochi, H., Umetani, K., Yagi, N. & Pearson, J. T. (2013). *Circ. Res.* **112**, 209–221.
Talbott, J. F., Whetstone, W. D., Readdy, W. J., Ferguson, A. R., Bresnahan, J. C., Saigal, R., Hawryluk, G. W., Beattie, M. S., Mabray, M. C., Pan, J. Z., Manley, G. T. & Dhall, S. S. (2015). *J. Neurosurg. Spine*, **3**, 495–504.
Tapfer, A., Braren, R., Bech, M., Willner, M., Zanette, I., Weitkamp, T., Trajkovic Arsic, M., Siveke, J. T., Settles, M., Aichler, M., Walch, A. & Pfeiffer, F. (2013). *PLoS One*, **8**, e58439.
Vågberg, W., Larsson, D. H., Li, M., Arner, A. & Hertz, H. M. (2015). *Sci. Rep.* **5**, 16625.
Velroyen, A., Bech, M., Zanette, I., Schwarz, J., Rack, A., Tympner, C., Herrler, T., Staab-Weijnitz, C., Braunagel, M., Reiser, M., Bamberg, F., Pfeiffer, F. & Notohamiprodjo, M. (2014). *PLoS One*, **9**, e109562.
Zhang, M. Q., Sun, D. N., Xie, Y. Y., Peng, G. Y., Xia, J., Long, H. Y. & Xiao, B. (2014). *Br. J. Radiol.* **87**, 20130670.
Zhao, T., Duan, F., Liao, X., Dai, Z., Cao, M., He, Y. & Shu, N. (2015). *Front. Hum. Neurosci.* **9**, 59.